Acta Materialia 135 (2017) 390–399

Contents lists available at ScienceDirect

Acta Materialia

journal homepage: www.elsevier.com/locate/actamat

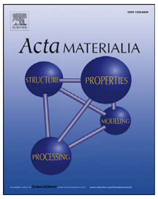

Full length article

Building blocks for a digital twin of additive manufacturing

G.L. Knapp [a], T. Mukherjee [a], J.S. Zuback [a], H.L. Wei [a], T.A. Palmer [a], A. De [b], T. DebRoy [a], *

[a] Department of Materials Science and Engineering, The Pennsylvania State University, University Park, PA, 16802, USA
[b] Department of Mechanical Engineering, Indian Institute of Technology, Bombay, 400076, India

ARTICLE INFO

Article history:
Received 11 April 2017
Received in revised form
20 June 2017
Accepted 20 June 2017
Available online 22 June 2017

Keywords:
3D printing
Deposit geometry
Solidification parameters
Secondary dendrite arm spacing
Micro-hardness

ABSTRACT

Properties and serviceability of additively manufactured components are affected by their geometry, microstructure and defects. These important attributes are now optimized by trial and error because the essential process variables cannot currently be selected from scientific principles. A recourse is to build and rigorously validate a digital twin of the additive manufacturing process that can provide accurate predictions of the spatial and temporal variations of metallurgical parameters that affect the structure and properties of components. Key building blocks of a computationally efficient first-generation digital twin of laser-based directed energy deposition additive manufacturing utilize a transient, three-dimensional model that calculates temperature and velocity fields, cooling rates, solidification parameters and deposit geometry. The measured profiles of stainless steel 316L and Alloy 800H deposits as well as the secondary dendrite arm spacing (SDAS) and Vickers hardness measurements are used to validate the proposed digital twin. The predicted cooling rates, temperature gradients, solidification rates, SDAS and micro-hardness values are shown to be more accurate than those obtained from a commonly used heat conduction calculation. These metallurgical building blocks serve as a phenomenological framework for the development of a digital twin that will make the expanding knowledge base of additive manufacturing usable in a practical way for all scientists and engineers.

1. Introduction

Properties and serviceability of metallic components produced by laser-assisted additive manufacturing (AM) depend on their geometry, microstructure and defects [1–5]. The evolution of microstructure and geometry is affected by the transient temperature fields, cooling rates and solidification parameters [6,7], which, in turn, depend on the process variables, alloy and specific AM process. Building a structurally sound and reliable component requires specification of an optimum set of process variables that affect the transient temperature fields, geometry and cooling rates.

Since there are many interrelated process variables, the selection of an optimized combination capable of producing a structurally sound, reliable component is challenging. The temperature fields and molten pool geometry are difficult to monitor and control in real time during AM. As a result, the structure and properties of components are routinely optimized by adjustment of many process variables by trial and error without any guiding scientific framework. Nearly all of the previous studies rely purely on empirical techniques in which select process parameters are varied while all others are held constant for achieving acceptable properties [8]. Post-process analyses determine the geometry, microstructure and mechanical properties of the as-built component. This approach is time consuming, expensive, and provides no assurance of attaining the optimal structure and properties of the component.

A recourse is to develop a phenomenological framework, or a digital twin [1], capable of predicting the most important variables that affect the metallurgical structure and properties of the components based on scientific principles. Ideally, the framework would enable users to specify any combination of AM process parameters and obtain the important metallurgical variables such as the transient temperature fields, molten pool geometry, temporal and spatial variations of cooling rates and solidification parameters rapidly. In principle, this digital twin of the AM process, when adequately validated with experimental data, would replace or reduce expensive, time-consuming physical experiments with rapid, inexpensive 'numerical experiments'. In the initial phase, such a model would consider all of the important AM process variables as input and provide the transient, three dimensional,

---

* Corresponding author.
E-mail address: debroy@psu.edu (T. DebRoy).

http://dx.doi.org/10.1016/j.actamat.2017.06.039

temperature and velocity fields, cooling rates, solidification parameters and geometry of the deposit as output. From these outputs, non-dimensional numbers, such as the thermal strain parameter, would be computed for further insight into the process [9–11].

Existing AM process models have their inherent advantages and disadvantages for specific applications. Finite element method based heat conduction models [12–14] are able to calculate deposit geometry and temperature distributions, from which heating and cooling rates can be extracted. However, these models neglect the effects of convective flow of molten metal inside the pool during the calculations of temperature distributions. This causes inaccurate predictions of melt pool shape, which leads to inaccuracies in cooling rates. For example, Manvatkar et al. [15] showed that by ignoring the effect of convection, the cooling rates in AM were overestimated by a factor of two. Svensson et al. [16] also noted that the use of a heat conduction equation did not adequately represent experimental cooling curves. Current heat transfer and fluid flow models [15,17] consider the Marangoni convection inside the pool by using a flat-surface assumption, allowing accurate estimation of the temperature and velocity distributions, cooling rates and solidification parameters. However, this assumption causes the predicted deposit geometry to deviate from experimental data. Level Set Method (LSM) [18] and Volume of Fluid (VOF) [19] method both track the evolution of the free surface of the deposit, thus, calculate the bead geometry. This advantage is offset by the fact that they are computationally intensive and often used for only two-dimensional calculations.

Here, we seek to develop and experimentally verify important building blocks for a first-generation digital twin of AM by developing a computationally efficient, comprehensive model with abilities to predict deposit geometry, transient temperature, velocity distributions and solidification parameters in three dimensions. An analytical sub-model based on mass conservation combined with consideration of powder catchment efficiency obtains an initial prediction of the deposit geometry with curved surfaces. A 3D transient heat transfer and fluid flow model provides a crucial building block needed for the prediction of all the important metallurgical variables that affect the structure and properties of the components. This model calculates temperature and velocity distributions, cooling rate and solidification parameters for a single-layer deposit. Experimental validation of the computed deposit geometry is undertaken for stainless steel 316L and Alloy 800H to demonstrate the applicability of the phenomenological digital twin to both alloy systems. Based on the calculated cooling rates, secondary dendritic arm spacing and hardness of SS 316L are calculated and compared with the corresponding experimental results. The actual tailoring of the final component's properties based on the predictive model is still a long way in the future and is outside the scope of this manuscript.

2. Theoretical calculations

2.1. Analytical calculations of the deposit geometry

Previous research on predicting single layer cladding geometry includes the use of parabolic and sinusoidal curves fitting [20], numerical algorithms [21], in-situ sensing [22], neural networks [20,23] and ANOVA techniques [24]. However, the curve-fitting calculations often rely solely on experimental observations and do not consider relevant phenomena such as mass conservation and material properties. In order to model the directed energy deposition (DED) process, the surface of the front edge of the deposit must be considered in three-dimensions. Experimentally, the leading edge of the deposit is located in front of the laser beam axis, which is likely due to a combination of powder-stream distribution and molten liquid spreading. Based on the success of parabolic function fits to 2D clad surfaces [20], an ellipsoidal function seems a natural extension for a 3D deposit surface. Behind the leading edge of the deposit, this profile reduces to an elliptical surface, such that the surface shape can be described for leading edge as,

$$\frac{x^2}{a^2}+\frac{y^2}{b^2}+\frac{z^2}{c^2}=1 \tag{1}$$

and behind the leading edge as,

$$\frac{y^2}{b^2}+\frac{z^2}{c^2}=1 \tag{2}$$

where a, b, and c are the principal axes of the ellipsoid, as depicted in Fig. 1. Taking advantage of the symmetry of the deposit along the x-z plane, half of the ellipsoid is used in the calculations to reduce computational costs. Physically, the values of b and c represent the deposit half-width and height, respectively, as shown in Fig. 1.

To calculate the values of a, b, and c, several simplifying assumptions are made:

1) The distribution of the blown powder stream is radially symmetric, and hence the values of a and b are equivalent.
2) For a particular alloy, the contact angle and the ratio of the height to half width (c/b) is constant.
3) The maximum deposit half-width is a fraction, f_m, of the laser beam radius, r_b. The value of f_m is calculated using heat balance,

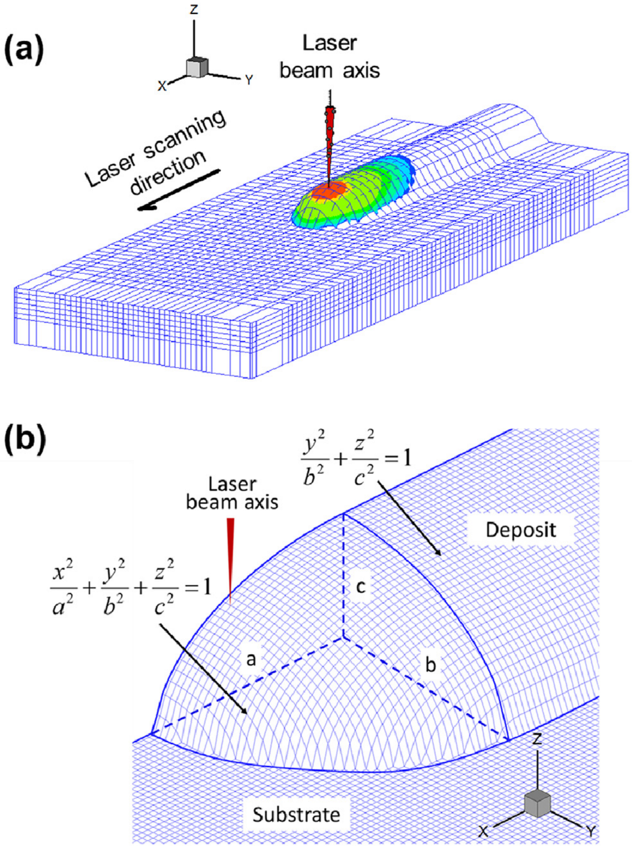

Fig. 1. (a) Schematic overview of the digital twin model. (b) Details of solution domain for the half-ellipsoid deposit indicating the position of the laser beam axis. Deposit is split along the symmetry plane for computational efficiency.

and its value typically varies between 0.75 and 1.0. If all of the supplied powders are included in the deposit, for example if the catchment efficiency is equal to 1.0, the value of f_m is also 1.0, and the half-width of the deposit is equal to r_b.

4) The radius of the powder stream is approximately equal to the laser beam radius at the substrate surface, which is typical of DED processes.

Considering the deposited mass must equal the mass of the deposited volume,

$$\eta_c\,\dot{m} = \frac{\pi}{2} b\; c v_s\; \rho \tag{3}$$

where η_c is the fractional mass catchment of powder into the pool, $\dot{m}$ is the powder mass flow rate from the nozzle, v_s is the scanning speed of the heat source, and ρ is the density of the deposit material. By assumption (3), $\dot{m}$ from Equation (3) can be rewritten as,

$$\dot{m} = \frac{\pi}{2} f_m\; r_b\; c_0\; v_s\; \rho \tag{4}$$

where, c_0 and $f_m r_b$ (*i.e.* b_0) are the maximum values of deposit height and half-width, respectively. By assumption (2) it is apparent that,

$$\frac{c}{b} = \frac{c_0}{f_m r_b} = \text{constant} \tag{5}$$

Therefore, Equation (3) can be solved for b and c as,

$$b = f_m\; r_b\; \sqrt{\eta_c} \tag{6}$$

$$c = \frac{2\;\dot{m}\;\sqrt{\eta_c}}{\pi\, f_m\; r_b\; v\; \rho} \tag{7}$$

From Equations (6) and (7), there is a clear need for an expression of the fractional mass catchment η_c. Previous studies of mass catchment into single bead deposits for powder-blown laser cladding [25–27] did not yield an analytical expression of η_c based on process parameters and material properties. However, intuition of the processes involved in powder entering the molten pool allows for the derivation of such an expression.

Huang et al. [28] have shown the catchment efficiency to be a function of the top surface area of the pool. Since pool size will grow with an increasing ratio of input energy to the amount of energy it takes to melt the material, catchment efficiency may be expressed as a function of a parameter Q,

$$Q = \frac{\left(P/_{v_s}\right)^{2/3}}{\left(C_P \Delta T + L\right)^{2/3}} \tag{8}$$

where P is laser power, v_s is scanning speed, C_p is specific heat, ΔT is the difference between the solidus temperature of the alloy and ambient temperature, and L is the latent heat of fusion of the alloy. To compare various experiments, it is preferable to take a normalized value of this parameter, Q^*, found by dividing Q by $Q_{\max}$ for the ensemble of data used. Therefore, η_c is calculated using a second order polynomial regression from both internal experimental data (see Section 3) and independent data from the literature [29] (Fig. 2), as,

$$\eta_c = \; -1.5\left(Q^*\right)^2 + 2.8\left(Q^*\right) - 0.3 \tag{9}$$

Using this value of the catchment efficiency, the magnitude of errors for the calculated width and height were 11.0% and 3.7%, respectively, when compared to corresponding experimental data (detailed results for geometry fitting are located in the Appendix). Minimal error in the calculation of the width and height of the beads for two different materials yielded a 95% confidence interval of ±15% for the value of η_c. While it is likely possible to refine the expression for η_c by adding more material parameters and experimental data to the model, the current form is applicable for practical estimations of mass catchment efficiency into the molten pool.

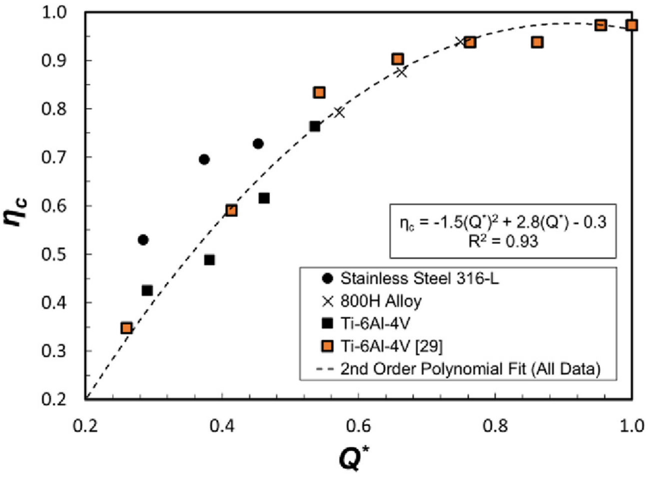

Fig. 2. Fitting of parameter Q^* to experimental data for the fractional mass catchment efficiency, η_c, into the molten pool [29].

2.2. Temperature and velocity field calculations

A three-dimensional numerical heat transfer and fluid flow model solves the enthalpy, three velocity components, and pressure fields for the geometry defined by Equations (6) and (7). The main assumptions of the model are the following. The density of the liquid metal has been assumed to be a constant except for the calculation of the buoyancy force in the momentum equation. This approximation, known as the Boussinesq approximation is widely used for the calculation of buoyancy driven flow [30,31]. Furthermore, the magnitude of the Marangoni force is higher than the buoyancy force by a factor of about 3000 [32]. In addition, the loss of alloying elements due to vaporization [33,34] and the resulting effect on both heat loss and composition change is ignored. The heat loss due to vaporization of alloying elements is a small fraction of the heat supplied by the laser beam for the conditions investigated in this paper. A short description of the calculation procedure is outlined in the supplementary materials.

The model is defined by the governing equations,

$$\frac{\partial(\rho u_i)}{\partial x_i} = 0 \tag{10}$$

$$\frac{\partial(\rho u_j)}{\partial t} + \frac{\partial(\rho u_j u_i)}{\partial x_i} = \frac{\partial}{\partial x_i}\left(\mu \frac{\partial u_j}{\partial x_i}\right) + S_j \tag{11}$$

where, ρ is the density, u_i and u_j are the velocity components along the i and j directions, respectively, and x_i is the distance along the i direction, t is the time, μ is the effective viscosity, and S_j is a source term for the momentum equation. In addition, the energy conservation equation is applied,

$$\rho\frac{\partial h}{\partial t}+\frac{\partial(\rho u_i h)}{\partial x_i}=\frac{\partial}{\partial x_i}\left(\frac{k}{C_p}\frac{\partial h}{\partial x_i}\right)-\rho\frac{\partial \Delta H}{\partial t}-\rho\frac{\partial(u_i\Delta H)}{\partial x_i} \tag{12}$$

where, h is the sensible heat, C_p is the specific heat, k is the thermal conductivity, and $\varDelta H$ is the latent heat content. Table 1 shows the thermo-physical properties of the alloys used for the calculations. Constant effective viscosity and effective thermal conductivity are taken as 2.0 and 3.0 times the nominal values, respectfully, to account for turbulence effects. Process parameters from Table 2 directly apply to the relevant simulations. A control volume method discretizes the governing equations by dividing the solution domain into small grids, with a total volume of 580 × 50 × 95 (length × width × height) grid points. The discretized equations are solved iteratively using the tri-diagonal matrix algorithm, and the calculations are completed using an in-house Fortran code. Typically, around 3.5 billion linear equations are solved for the deposition of one layer, which takes approximately 50 min in a personal computer with 3.40 Gigahertz i7 processor and 8 Gigabyte RAM (random access memory).

The model considers the laser as a Gaussian-distributed heat source centered at a distance of ½a from the leading edge of the deposit, as shown in Fig. 1. In DED, the powder particles absorb heat during their flight from the nozzle to the substrate, so the applied energy density consists of a volumetric flux term and a surface flux term. The volumetric term, distributed from the surface of the deposit down to the top of the substrate, represents the heat absorbed by the powder during flight.

$$S_V=\frac{Q_V d}{\pi r_b^2 c}\exp\left(-d\frac{r^2}{r_b^2}\right) \tag{13}$$

where Q_v is the total heat absorbed by the powder per unit time during their flight, d is the laser beam intensity distribution factor, c is the height of the deposit (see Fig. 1), r_b is the focused laser beam radius, and r is the radial distance from the beam axis. It is assumed that, on average, the powder particles are heated to solidus temperature during flight, such that:

$$Q_V=\dot{m}c_p(T_{solidus}-T_{ambient}) \tag{14}$$

The remaining energy is applied as a surface flux term, S_s, as shown below:

$$S_S=\frac{Q_S d}{\pi r_b^2 c}\exp\left(-d\frac{r^2}{r_b^2}\right) \tag{15}$$

where Q_s is the net available power that is applied on the deposit surface. Energy conservation is observed such that:

$$Q_V+Q_S=\eta P \tag{16}$$

where P is the nominal laser power and η is the absorptivity of the powder particles that varies between 0.3 and 0.7 [35].

The boundary conditions for the thermal analysis include heat loss by convection and radiation to the surroundings. Spatial variation in pool surface temperature creates a surface tension gradient that drives the convective flow of molten metal inside the pool. The temperature gradient along the 3D curved surface (G) has three components along the x−, y−, and z−directions (G_x, G_y, G_z, respectively). The Marangoni stress at any point on the curved surface along the x−, y−, and z−directions, respectively, is,

$$\tau_x=\mu\frac{du}{dz}=\frac{d\gamma}{dT}G_x \tag{17}$$

$$\tau_y=\mu\frac{dv}{dz}=\frac{d\gamma}{dT}G_y \tag{18}$$

$$\tau_z=\mu\frac{dw}{dr}=\frac{d\gamma}{dT}G_z \tag{19}$$

where T is the temperature, γ is the surface tension, μ is the viscosity of the liquid metal, r is the radial distance from the central axis of the heat source, and u, v, and w are the velocities of the liquid metal along the x−, y−, and z−directions, respectively.

During the calculation of the temperature fields, the molten pool geometry and peak temperature are extracted, which allows for the calculation of the non-dimensional thermal strain parameter described by Mukherjee et al. [10]. This parameter allows for the comparison of the relative amount of thermal distortion between materials and processes.

3. Experimental investigations

A series of 76 mm long single pass, single layer builds were deposited using pre-alloyed SS 316L and 800H powders (Carpenter Powder Products, Inc.) on a 150 mm × 150 mm x 12.7 mm annealed substrate of similar alloy as that of the powder. The powders were gas atomized in nitrogen and had a mesh size range of −100/+325, meaning that the diameter of each powder particle was between 45 and 145 μm. Laser powers ranging from 1000 to 3000 W were used to deposit the builds while all other parameters were kept constant. The process parameters used for the depositions are given in Table 2. The specimens were fabricated using a custom-designed, in-house laser assisted directed energy deposition (DED-L) system with a controlled environment. The build chamber was purged with high purity argon to reduce oxygen levels during experiments. A ytterbium fiber laser (IPG Photonics® YLR-12000-L) with a wavelength of approximately 1080 nm was supplied to the

Table 1
Thermo-physical properties of SS 316L and Alloy 800H.

Properties	SS 316L	800H
Liquidus temperature (K)	1733	1607
Solidus temperature (K)	1693	1674
Thermal conductivity (W/m K)	11.82 + 0.0106 T	8.54 + 0.0167 T
Specific heat (J/kg K)	330.9 + 0.563 T − 4.015 × 10^{-4} T^2 + 9.465 × 10^{-8} T^3	309.2 + 0.5104 T
Density (kg/m^3)	7800	7870
Volumetric expansion co-efficient (/K)	5.85 × 10^{-5}	1.02 × 10^{-5}
Viscosity (kg/m s)	7 × 10^{-3}	7.4 × 10^{-3}
dγ/dT (N/m K)	−0.40 × 10^{-3}	−0.24 × 10^{-3}
Surface tension (N/m)	1.50	1.69
Latent heat of fusion (J/kg)	2.72 × 10^5	2.65 × 10^5

Table 2
Key experimental and simulation process parameters.

Alloy	Laser power (W)	Beam radius (mm)	Scanning speed (mm/s)	Substrate thickness (mm)	Powder flow rate (g/s)
SS 316L	1000–2500	2.0	10.6	10	0.25
Alloy 800H	1500–3000	2.0	10.6	10	0.25

chamber through a reflective optics system. Powder was delivered through four separate nozzles, each of which measuring approximately 1.6 mm in diameter at the point of exit.

A transverse cross section approximately 4 mm thick was removed near the middle of each deposit using an abrasive cutting wheel with a silicon carbide blade. A series of silicon carbide papers up to 1200 grit and metallographic polishing with 3 and 1 μm polycrystalline diamond suspension followed by a final polishing with 0.05 μm colloidal silica was used to obtain a mirror finish. Electrolytic etching was performed on the SS 316L samples with 10% oxalic acid at 5 V for approximately 3 s to reveal grain boundaries and sub-grain structure.

Micro-hardness measurements were taken using a Vickers indenter on a LECO M-400-G1 machine. Each indentation was subjected to a 300 g load at a dwell time of 5 s. Hardness measurements were spaced uniformly throughout the deposit, including the dilution region into the substrate. Light optical microscopy and scanning electron microscopy (SEM) on an FEI Quanta 200 machine were used to view the deposit geometry and grain structure of the transverse cross sections. SEM images were taken in both secondary electron and backscatter electron modes using a 20 kV accelerating voltage and 4 mm spot size. Secondary dendritic arm spacing (SDAS) was measured by image analysis techniques using ImageJ. Grayscale values were measured along a linear path intersecting multiple secondary dendrites. A peak value corresponded to the inter-dendritic regions that were shown in bright contrast on SEM images due to the elemental redistribution of heavier elements. The distance between each peak was then used to determine the approximate center of a secondary dendrite arm, which was ultimately used to calculate the SDAS.

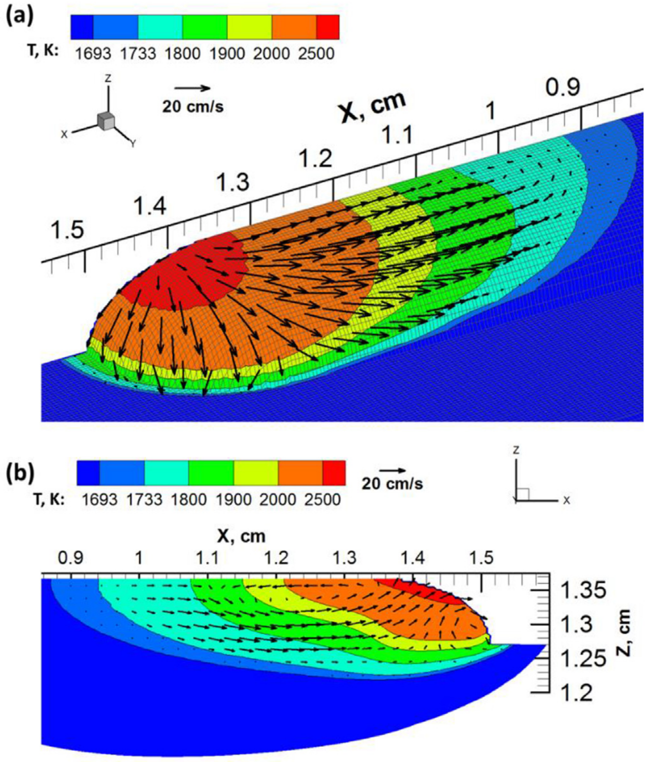

Fig. 3. Temperature and velocity distributions on the curved shaped deposit for stainless steel 316L at 2500 W laser power (a) 3D isometric view and (b) longitudinal sectional view, where the scanning direction is along the positive x-axis.

4. Results and discussion

Fig. 3(a) and (b) show the computed temperature and the velocity distributions on the three-dimensional curved surface and along the longitudinal section of the SS 316L deposit, respectively. The color bands represent the ranges of temperatures corresponding to the figure legend. The location of the peak temperature is near the laser beam axis. The scanning direction is along the positive x-axis. Due to the rapid scanning of the heat source, the isotherms behind the laser beam axis are elongated while the isotherms ahead of the laser beam are compressed. The velocity vectors of the molten metal inside the pool are shown by arrows. A reference vector is shown by an arrow and a comparison of the length of this arrow with the vectors in the plots indicates the relative magnitudes of the computed velocities. The convective flow of liquid metal is primarily driven by the Marangoni stresses caused by the surface tension gradient due to the temperature difference on the surface of the molten pool. Therefore, on the top surface of the deposit the molten metal flows from the high temperature region to the low temperature region along the curved surface as shown in Fig. 3(a). This fluid flow is responsible for enthalpy transport from the front of the pool to the rear, elongating the thermal contours at the back of the pool. Calculated Peclet numbers ranged from 6.3 at 1000 W to 13.4 at 2500 W for SS 316L, showing the increasing role of convective heat transport as heat input, and therefore the magnitude of the Marangoni stresses, increases.

Fig. 3(b) shows that the pool is deeper and has higher temperature and velocities towards the front. Towards the trailing edge of the pool, velocities decrease and the direction of flow is no longer dominated by Marangoni stresses since the temperature gradients are lower at these locations. As velocity diverges from the location of the heat source, separate convective loops are formed, as seen in the front, side, and back of the pool in Fig. 4(a–d). Because of this divergence from the heat source center, the assumed geometry of the deposit and heat source are important in determining the path of fluid convection.

Fig. 5(a) and (b) show the comparisons between the computed transverse section of the deposit with the corresponding experimentally measured macrograph of SS 316L deposits using 1500 W and 2500 W laser powers, respectively. In both figures, the pool boundary is shown as the solidus temperature contour of 1693 K, the mushy zone is shown in orange for temperatures between solidus and liquidus (1733 K) temperatures, and the fusion zone of the deposit is depicted in red for the region heated above the liquidus temperature. Both figures show fair agreements between the computed and the corresponding experimentally measured results. The temperature at the center of the deposit is higher than that of the sides, so molten metal flows from the center of the deposit to the sides along the curved top surface, as shown in Fig. 5. Higher laser power can melt more powders. Therefore, the deposit

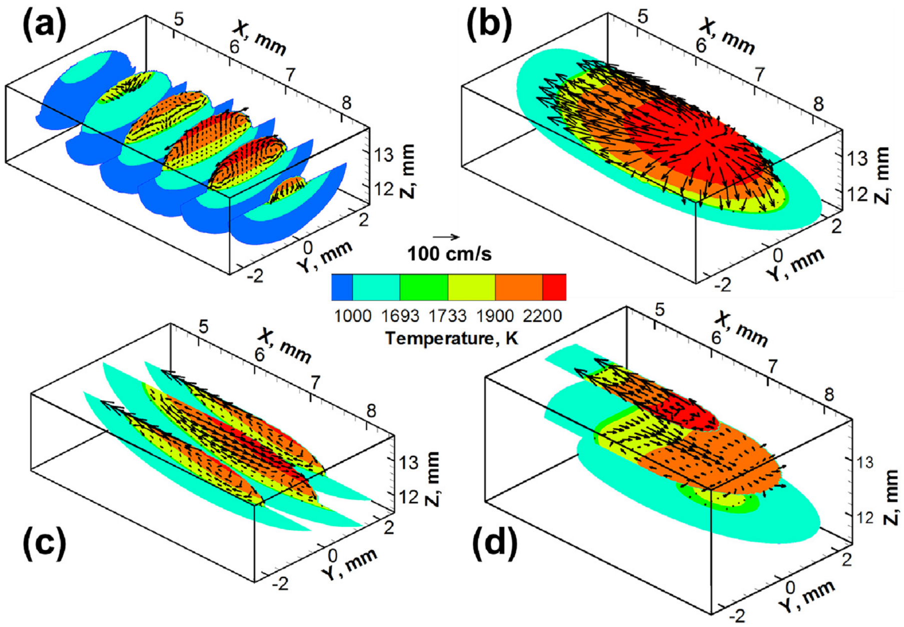

Fig. 4. An instantaneous view of multiple sections through the deposit from simulated stainless steel 316-L at 2500 W laser power: (a) horizontal sections, (b) top-surface, (c) longitudinal sections, and (d) transverse sections. The leading edge of the bead is at x = 8.5 mm.

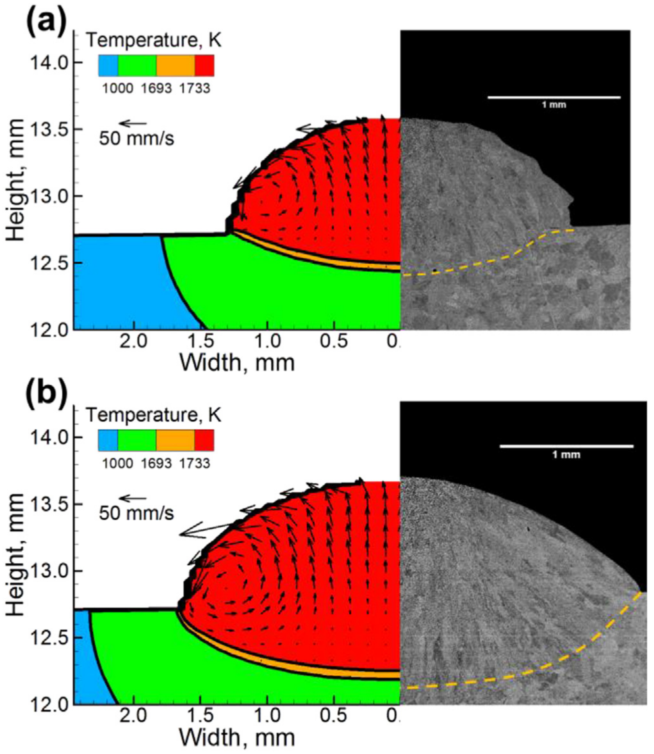

Fig. 5. Comparison of the calculated deposit shape and size with experimental macrograph at the transverse cross section of the build for stainless steel 316L at (a) 1500 W and (b) 2500 W laser power. The dotted lines indicates the edge of the dilution region.

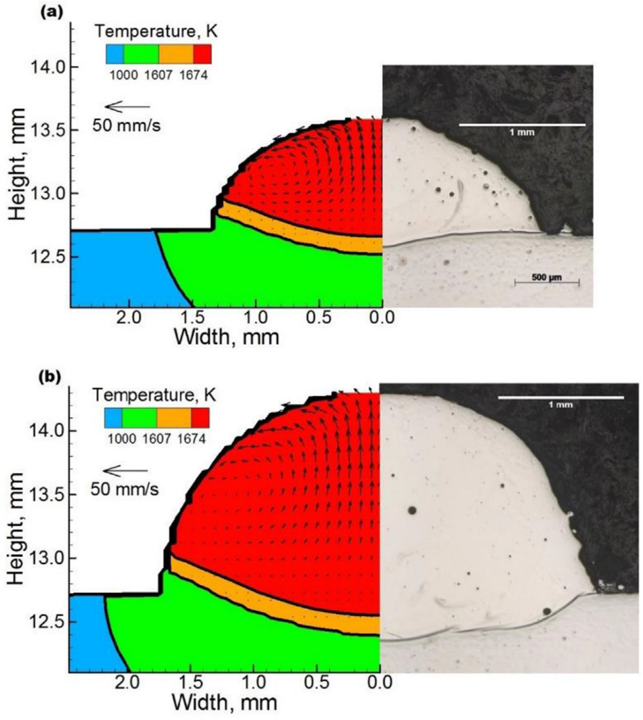

Fig. 6. Comparison of the calculated deposit shape and size with experimental macrograph at the transverse cross section of the build for Alloy 800H at (a) 1500 W and (b) 2500 W laser power.

fabricated using 2500 W laser power is larger than that produced with 1500 W. Fig. 6(a) and (b) also show the comparisons between the computed transverse section of the deposit with the corresponding macrograph using 1500 W and 2500 W laser powers, respectively, for Alloy 800H deposits. Similar observations can be made in these figures. However, Alloy 800H has a lower liquidus temperature than that of SS 316L. Under the same heat input, the amount of the molten material will be more for Alloy 800H, resulting in a larger deposit for Alloy 800H.

Fig. 7 shows the computed variation of the temperature with respect to time, as monitored at the mid height of the deposit center while fabricating 1 cm long SS 316L and Alloy 800H samples

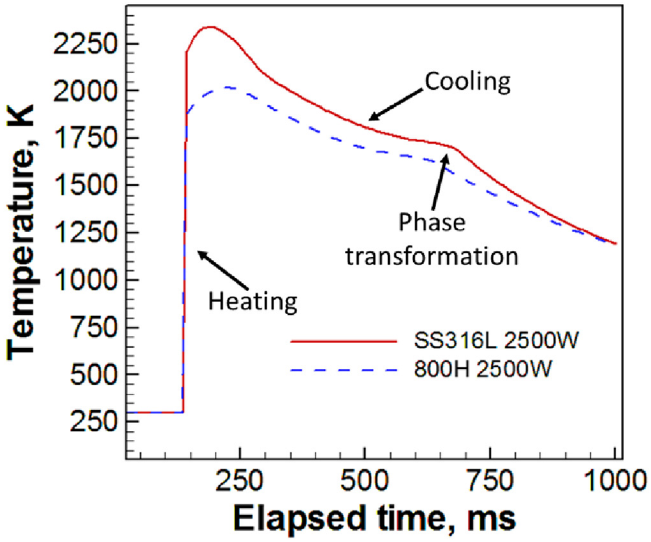

Fig. 7. Simulated thermal history for a location approximately a fifth of the way along the 1.0 cm long deposit length of SS 316L at 2500 W.

using 2500 W laser power. Alloy 800H has higher thermal diffusivity than that of SS 316L, so the peak temperature attained by the SS 316L deposit is higher than that of Alloy 800H. From this figure, it can be observed that heating occurs very rapidly, however the cooling is relatively slower. During the cooling, there is a sudden change in the slope of the curve, representing the solid-to-liquid phase transformation. The slope of the curve during the cooling represents the cooling rate as the build solidifies. For example, in Fig. 7, the calculated cooling rates during solidification are the slope of the curve between the liquidus and solidus temperature. As temperature histories can be stored for any arbitrary point in the model, cooling rates can be determined both spatially and temporally.

Fig. 8(a) and (b) show the comparison of the current model with a heat conduction model and a model with flat a surface assumption, in terms of predicting cooling rate and G/R ratio at different laser powers. With the increase of laser power, pool size increases, which causes the temperature gradients to decrease due to the spreading of isotherms. Therefore, for the same material subjected to similar process parameters, cooling rate and G/R values decrease with higher power. A reduced G/R value indicates that the solidification front will be less stable and columnar to equiaxed transition may occur. As the heat conduction model neglects the mixing of hot and cold liquid by convection, it overestimates the temperature gradient. Therefore, the calculated cooling rate using the heat conduction model is about twice of that calculated using the current model.

Experimental SDAS and hardness measurements of the SS 316L, found in Table 3, show an increase in arm spacing, from 2.51 ± 0.67 μm at 1000 W to 3.27 ± 0.65 μm at 2500 W, and decrease in Vickers hardness as laser power increases, from 214.6 ± 2.2 HV at 1000 W to 205.3 ± 3.2 HV at 2500 W. SEM imaging of the SDAS in Fig. 9 shows the increased arm spacing when using 2500 W compared to 1500 W. To compare the experimental results to the simulated cooling rates, empirical equations for deriving micro-hardness values from cooling rate are taken from literature. First, SDAS is calculated from cooling rate, followed by yield strength calculated from SDAS. Finally, an average micro-hardness is calculated from yield strength. The average magnitude of SDAS of powder-blown AM stainless steel components can be represented as [36],

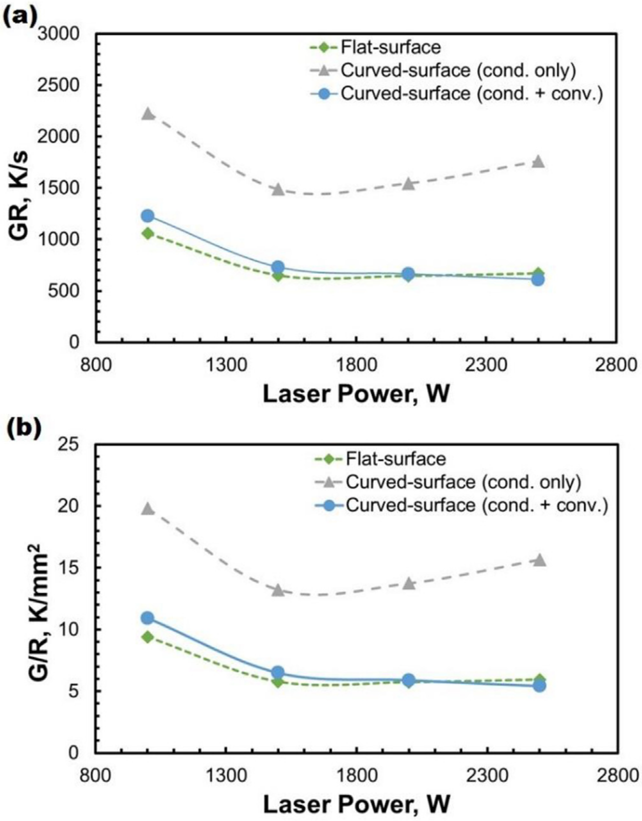

Fig. 8. Comparison of the calculations of (a) cooling rate and (b) temperature gradient to growth rate ratio (G/R) using the current model, flat surface model and heat conduction model for DED of SS 316L at different laser power.

$$\lambda = 50(GR)^{-0.4} \tag{20}$$

where, λ is the SDAS in μm, and GR is the cooling rate in K/s. For very fine columnar dendritic structure, the yield strength can be correlated with SDAS as [15],

$$\sigma_y = \sigma_0 + K_y(\lambda)^{-0.5} \tag{21}$$

Where σ_0 and K_y are constants whose values for SS 316L are 240 MPa and 279 MPa $(\mu m)^{0.5}$, respectively [37]. The average micro-hardness of SS 316 is related to the yield strength as [15],

$$H_v = 3\sigma_y(0.1)^{-0.25} \tag{22}$$

Applying simulated values of GR from Fig. 8 to Equations (20)–(22) yields the average micro-hardness values presented in Fig. 10, which agree with experimentally measured values, within experimental error. Calculated hardness values for the curved-surface model without fluid convection are significantly higher than the measured experimental values, confirming that fluid convection is a necessary phenomenon to consider when modeling additive manufacturing processes. Without it, the cooling rates become significantly greater due to lack of heat transfer from the front of the pool to the rear, and any properties calculated based on cooling rates will be erroneous.

Finally, the analysis of the thermal strain parameter, ε^*, was carried out in the manner recently proposed by Mukherjee et al. [5]. The thermal strain parameter is stated to be a function of laser speed, laser power, and deposit geometry as [5].

Table 3
Experimental measurements of secondary dendritic arm spacing and Vickers hardness for SS 316L samples.

Laser Power (W)	SDAS (μm)	SDAS Standard Deviation (μm)	Vickers Hardness (HV)	Vickers Hardness Standard Deviation (HV)
1000	2.51	0.67	214.6	2.24
1500	3.19	0.73	211.4	1.85
2000	3.01	0.93	211.2	2.79
2500	3.27	0.65	205.3	3.23

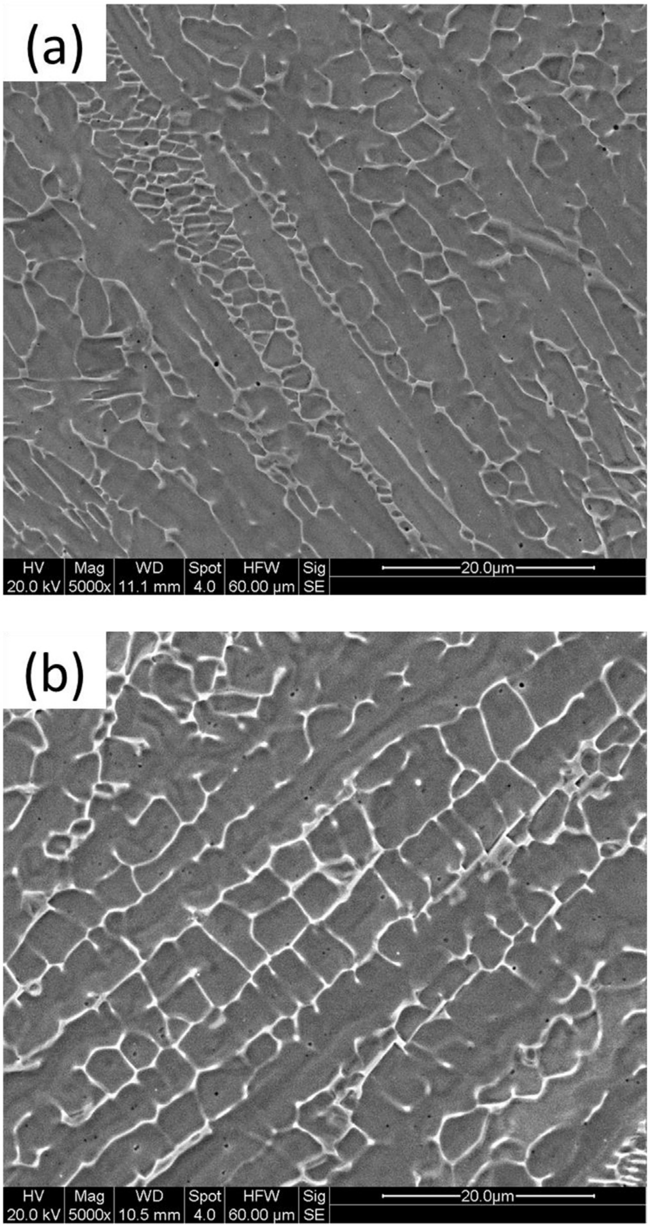

Fig. 9. Scanning electron microscopy image at the transverse cross section of SS 316L build using (a) 1500 W and (b) 2500 W laser power.

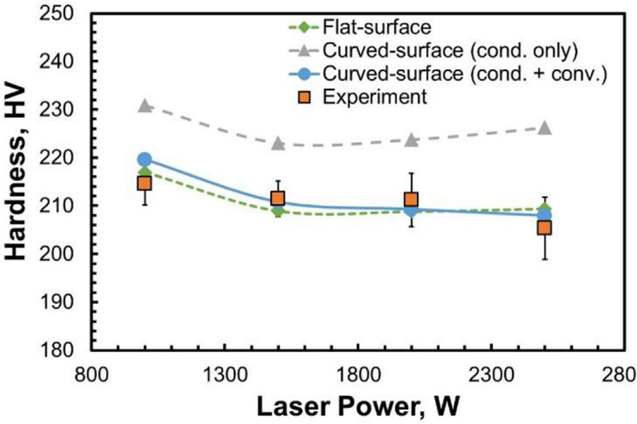

Fig. 10. Comparison of calculated average micro-hardness of stainless steel 316L at various laser powers with experimental data. Error bars are two of the standard deviations calculated for each dataset, in each direction.

$$\varepsilon^* = \frac{\beta \Delta T}{EI} \frac{t}{F\sqrt{\rho}} H^{3/2} \tag{23}$$

where EI is the flexural rigidity of the substrate plate, $\beta \Delta T$ is the volumetric change, t is the deposition time, ρ is the density, F is the Fourier number, and H is the heat input per unit length. Applying Equation (23) to SS 316L and Alloy 800H (Fig. 11) revealed that for both increasing laser powers and scanning speeds, Alloy 800H has a lower ε^* than SS 316L. This is a qualitative result, showing that Alloy 800H is less susceptible to thermal distortion and dimensional inconsistency defects than SS 316L. The sharp increase in ε^* for SS 316L at lower scanning speeds indicates a higher potential for defects with decreasing scanning speed, while Alloy 800H appears to be more resilient to changes in scanning speed. These results show the usefulness of being able to compute the thermal strain parameter for various materials, as the appropriateness of various processing parameters can be determined for each material. While the exact amount of thermal distortion requires more complex modeling, calculations of ε^* allow precautions to be taken to prevent thermal distortion by proper material and/or parameter selection.

5. Summary and conclusions

Building blocks for developing a digital twin of the AM process will utilize a transient, three-dimensional model that calculates temperature and velocity fields, cooling rates, solidification parameters and deposit geometry. This model is proposed, then validated with experimental data of single-pass, single-layer deposits. The following are the most important findings.

(1) The proposed building blocks of a first-generation digital twin of AM have been assembled to accurately estimate 3D curved surface deposit geometry for single-pass deposits, transient temperature and velocity distributions, cooling rates, solidification parameters, secondary dendrite arm spacing and micro-hardness in a computationally efficient manner. Use of the proposed framework will minimize the time consuming and expensive empirical tests to evaluate the effects of the process variables on cooling rates, single-layer deposit geometry and some structural features.

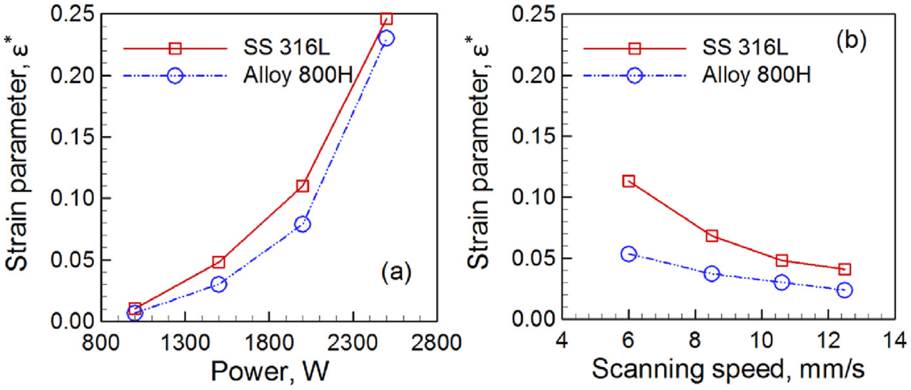

Fig. 11. Calculated thermal strain parameter for SS 316L and Alloy 800H with varying (a) laser power and (b) laser scanning speed.

Table A1
Comparison between estimated and calculated width and height of the deposit.

Material	Laser Power, W	f_m	Calculated width, mm (% error from measured value)	Calculated height, mm (% error from measured value)
SS 316L	1000	0.82	2.23 (−20%)	0.85 (0%)
SS 316L	1500	0.87	2.64 (+4%)	0.90 (+1%)
SS 316L	2000	0.91	2.96 (+16%)	0.92 (+4%)
SS 316L	2500	0.94	3.19 (−16%)	0.93 (−4%)
800H	2000	0.945	3.38 (+12%)	1.44 (−6%)
800H	2500	0.97	3.65 (+6%)	1.48 (−7%)
800H	3000	0.99	3.84 (−3%)	1.49 (−4%)
Average Magnitude of Error:			11.0%	3.7%

Further work could extend these results into a true digital twin capable of accounting for larger-scale factors, such as part geometry.

(2) It is found that the catchment efficiency of the powders increases with higher heat input owing to an increase in molten pool top surface area. A simple analytical model is proposed to predict the catchment efficiency based solely on process parameters and the material properties, enabling back-of-the-envelope calculations that were previously absent in literature.

(3) The convective flow of the molten metal driven by the Marangoni stresses along the curved surface of the deposit significantly changes the temperature distribution, cooling rates and solidification parameters. Mechanical properties such as micro-hardness and secondary dendritic arm spacing can be predicted from the calculated solidification parameters.

(4) Calculation of pool geometry, temperature and velocity fields, and solidification parameters allows for the calculation of many dimensionless numbers. These provide insight into the relative differences of structure, property, and defects expected while doing additive manufacturing of different materials. As an example, calculation of the dimensionless thermal strain parameter, ε^*, shows that SS 316L is more susceptible to thermal distortion defects than Alloy 800H.

Acknowledgements

We acknowledge the support from the Department of Energy Nuclear Energy University Program grant number DE-NE0008280. One of the authors acknowledges support of an American Welding Society research fellowship, grant number 179466.

Appendix A. Supplementary data

Supplementary data related to this article can be found at http://dx.doi.org/10.1016/j.actamat.2017.06.039.

Appendix B. Calculation of maximum deposit width

This appendix details how to calculate the maximum deposit half-width as a fraction, f_m, of the laser beam radius, r_b. The value of f_m is calculated using heat balance, assuming that for a laser with a Gaussian distribution there is some point along the beam radius where the energy density is too small to melt the powder being placed on the substrate.

The upper limit of the value of f_m is 1.0, as the effective energy density outside of the beam radius is zero. Within the laser radius, the power distribution of a laser of nominal power P can be defined as $f(x,y)$, which is typically a bivariate normal distribution function (*i.e.* Gaussian distribution). The limiting factor for laser energy density is that the total energy incident on any one particle of deposit material is greater than or equal to the amount of energy required to melt the particle. The total energy deposited on the particle is expressed as,

$$E_p = (\Delta t^* P)\left(\frac{l}{2r_b}\right)\int_{r}^{r+l}\int_{-r_b}^{r_b} f(x,y)dx\,dy \qquad \text{(A1)}$$

where, laser travel is along the x-axis at scanning speed v_s, r is the distance from the center of the beam, Δt is the total time the laser beam is incident on the particle, and l is the side-length of a small square area the laser is incident upon. As particles are generally spherical, l is a function of particle diameter D_p as,

$$l = \sqrt{\pi}\left(\frac{D_p}{2}\right) \tag{A2}$$

In this scenario, the time Δt it takes the entire laser to pass over one particle is,

$$\Delta t = \frac{2r_b}{v_s} \tag{A3}$$

The amount of energy required to melt a single spherical particle is,

$$E_{req} = \frac{4}{3}\pi\left(\frac{D_p}{2}\right)^3 \rho\left(C_p\left(T_s - T_p\right) + L\right) \tag{A4}$$

where T_s is the solidus temperature and T_p is the preheat temperature. By using a graphical approach to solve $E_P = E_{req}$ for the critical radius $r = r_{crit}$ the maximum deposit width is,

$$r_{crit} = r_b f_m \rightarrow f_m = \frac{r}{r_b} \tag{A5}$$

Now using Equations (6) and (7) the half width b and the height c are calculated for each experimental trial and compared to the experimental measurements. Table A1 presents the results of those calculations, showing that on average the width deviated by 11.0% of the measured experimental value while the height deviated by approximately 3.7%.

References

[1] T. DebRoy, W. Zhang, J. Turner, S.S. Babu, Building digital twins of 3D printing machines, Scr. Mater. 134 (2017) 61–65.

[2] D.D. Gu, W. Meiners, K. Wissenbach, R. Poprawe, Laser additive manufacturing of metallic components: materials, processes and mechanisms, Int. Mater. Rev. 57 (3) (2012) 133–164.

[3] B.E. Carroll, T.A. Palmer, A.M. Beese, Anisotropic tensile behavior of Ti-6Al-4V components fabricated with directed energy deposition additive manufacturing, Acta Mater. 87 (2015) 309–320.

[4] Z. Wang, T.A. Palmer, A.M. Beese, Effect of processing parameters on microstructure and tensile properties of austenitic stainless steel 304L made by directed energy deposition additive manufacturing, Acta Mater. 110 (2016) 226–235.

[5] T. Mukherjee, J.S. Zuback, A. De, T. DebRoy, Printability of alloys for additive manufacturing, Sci. Rep. 6 (2016) 19717.

[6] H.L. Wei, J.W. Elmer, T. DebRoy, Three-dimensional modeling of grain structure evolution during welding of an aluminum alloy, Acta Mater. 126 (2017) 413–425.

[7] H.L. Wei, J.W. Elmer, T. DebRoy, Origin of grain orientation during solidification of an aluminum alloy, Acta Mater. 115 (2016) 123–131.

[8] H. Gong, K. Rafi, H. Gu, T. Starr, B. Stucker, Analysis of defect generation in Ti-6Al-4V parts made using powder bed fusion additive manufacturing processes, Addit. Manuf. 1 (2014) 87–98.

[9] T. Mukherjee, W. Zhang, T. DebRoy, An improved prediction of residual stresses and distortion in additive manufacturing, Comp. Mater. Sci. 126 (2017) 360–372.

[10] T. Mukherjee, V. Manvatkar, A. De, T. DebRoy, Mitigation of thermal distortion during additive manufacturing, Scr. Mater. 127 (2017) 79–83.

[11] T. Mukherjee, V. Manvatkar, A. De, T. DebRoy, Dimensionless numbers in additive manufacturing, J. Appl. Phys. 121 (6) (2017) 064904.

[12] N.E. Hodge, R.M. Ferencz, J.M. Solberg, Implementation of a thermomechanical model for the simulation of selective laser melting, Comp. Mech. 54 (1) (2014) 33–51.

[13] P. Prabhakar, W.J. Sames, R. Dehoff, S.S. Babu, Computational modeling of residual stress formation during the electron beam melting process for Inconel 718, Addit. Manuf. 7 (2015) 83–91.

[14] K. Zeng, D. Pal, H.J. Gong, N. Patil, B. Stucker, Comparison of 3DSIM thermal modelling of selective laser melting using new dynamic meshing method to ANSYS, Mater. Sci. Technol. 31 (8) (2015) 945–956.

[15] V. Manvatkar, A. De, T. DebRoy, Heat transfer and material flow during laser assisted multi-layer additive manufacturing, J. Appl. Phys. 116 (12) (2014) 124905.

[16] L.E. Svensson, B. Gretoft, H.K.D.H. Bhadeshia, An analysis of cooling curves from the fusion zone of steel weld deposits, Scand. J. Metall. 15 (1986) 97–103.

[17] V. Manvatkar, A. De, T. DebRoy, Spatial variation of melt pool geometry, peak temperature and solidification parameters during laser assisted additive manufacturing process, Mater. Sci. Technol. 31 (8) (2015) 924–930.

[18] H. Qi, J. Mazumder, H. Ki, Numerical simulation of heat transfer and fluid flow in coaxial laser cladding process for direct metal deposition, J. Appl. Phys. 100 (2) (2006) 024903.

[19] Y. Lee, M. Nordin, S.S. Babu, D.F. Farson, Effect of fluid convection on dendrite arm spacing in laser deposition, Metall. Mater. Trans. B 45 (4) (2014) 1520–1529.

[20] Y. Cao, S. Zhu, X. Liang, W. Wang, Overlapping model of beads and curve fitting of bead section for rapid manufacturing by robotic MAG welding process, Robot. CIM-Int. Manuf. 27 (3) (2011) 641–645.

[21] M. Alimardani, E. Toyserkani, J.P. Huissoon, Three-dimensional numerical approach for geometrical prediction of multilayer laser solid freeform fabrication process, J. Laser Appl. 19 (1) (2006) 14–25.

[22] C. Doumanidis, Y.-M. Kwak, Multivariable adaptive control of the bead profile geometry in gas metal arc welding with thermal scanning, Int. J. Pres. Ves. Pip. 79 (4) (2002) 251–262.

[23] J. Xiong, G. Zhang, J. Hu, L. Wu, Bead geometry prediction for robotic GMAW-based rapid manufacturing through a neural network and a second-order regression analysis, J. Intell. Manuf. 25 (1) (2014) 157–163.

[24] D.J. Corbin, A.R. Nassar, E.W. Reutzel, A.M. Beese, N.A. Kistler, Effect of directed energy deposition processing parameters on laser deposited Inconel® 718: external morphology, J. Laser Appl. 29 (2) (2017) 022001.

[25] S. Carty, I. Owen, W.M. Steen, B. Bastow, J.T. Spencer, Catchment efficiency for novel nozzle designs used in laser cladding and alloying, in: J. Mazumder, O. Conde, R. Villar, W. Steen (Eds.), Laser Processing: Surface Treatment and Film Deposition, Springer, Netherlands, 1996, pp. 395–410.

[26] K. Partes, Analytical model of the catchment efficiency in high speed laser cladding, Surf. Coat. Technol. 204 (3) (2009) 366–371.

[27] H.K. Lee, Effects of the cladding parameters on the deposition efficiency in pulsed Nd:YAG laser cladding, J. Mater. Process. Tech 202 (1–3) (2008) 321–327.

[28] Y. Huang, M.B. Khamesee, E. Toyserkani, A comprehensive analytical model for laser powder-fed additive manufacturing, Addit. Manuf. 12 (2016) 90–99.

[29] R.M. Mahamood, E.T. Akinlabi, M. Shukla, S. Pityana, Material efficiency of laser metal deposited Ti6Al4V: effect of laser power, Eng. Lett. 21 (1) (2013).

[30] J.S. Turner, Buoyancy Effects in Fluids, Cambridge University Press, 1979.

[31] Z. Fan, F. Liou, Numerical modeling of the additive manufacturing (AM) process of titanium alloy, in: A.K.M. Nural Amin (Ed.), Titanium Alloys—towards Achieving Enhanced Properties for Diversified Applications, InTech, Croatia, 2012, pp. 3–28.

[32] W. Zhang, Probing Heat Transfer, Fluid Flow and Microstructural Evolution during Fusion Welding of Alloys, Department of Materials Science and Engineering, The Pennsylvania State University, 2004.

[33] P.A.A. Khan, T. Debroy, Alloying element vaporization and weld pool temperature during laser welding of AISI 202 stainless steel, Metall. Trans. B 15 (1984) 641–644.

[34] M. Collur, A. Paul, T. DebRoy, Mechanism of alloying element vaporization during laser welding, Metall. Trans. B 18 (1987) 733–740.

[35] A. Raghavan, H.L. Wei, T.A. Palmer, T. DebRoy, Heat transfer and fluid flow in additive manufacturing, J. Laser Appl. 25 (5) (2013) 052006.

[36] H. Yin, S.D. Felicelli, Dendrite growth simulation during solidification in the LENS process, Acta Mater. 58 (4) (2010) 1455–1465.

[37] B.P. Kashyap, K. Tangri, On the Hall-Petch relationship and substructural evolution in type 316L stainless steel, Acta Metall. Mater. 43 (11) (1995) 3971–3981.